LIF-thermometry with MDR-enhanced energy transfer for micro-droplet temperature imaging for varying ambient pressures

Leif Schumacher*, Johannes Palmer, Valeri Kirsch, Manuel A. Reddemann, Reinhold Kneer

[1]Institute of Heat and Mass Transfer, RWTH Aachen University, Germany
*Corresponding author: schumacher@wsa.rwth-aachen.de

Abstract
A relatively new method called pulsed 2D-2cLIF-EET is applied for temperature imaging of heated micro droplets. The method uses laser induced fluorescence (LIF) to determine the local temperature field in droplets. Due to the application of a pulsed laser the planar imaging of moving droplets is not restricted to motion blur anymore. Enhanced energy transfer (EET) is used to prevent dye-lasing and makes LIF-thermometry possible even with high excitation energies of pulsed lasers. The system offers an average droplet temperature accuracy of 0.5 K and a spatial median absolute deviation of approximately 2.5 K. The local temperature values of every pixel represent an integral temperature along the droplet depth. Thus, the three dimensional temperature field is averaged and projected onto two dimensions (planar). The system is used to measure the planar temperature field of a n-dodecane droplet stream in hot gas atmosphere. Experiments are conducted with ambient pressures of 1.39 bar and 2.11 bar. The raising ambient pressure influences the convective heat transfer at the droplet surface (increased by around 15 %) and thereby heat transfer into the droplet. The temperature distribution inside the droplet does not show the typical structure of a Hill-vortex, which would be characteristic for the flow inside a moving droplet. Comparison with the "effective thermal conductivity model" for a monodisperse droplet stream shows good agreement for the low ambient pressure, but deviations for the elevated pressure.

Keywords
droplet heating, temperature imaging, 2cLIF, heat transfer

Introduction

Evaporation and heating of micro droplets are key processes in a variety of technical applications, e.g. for efficient internal combustion engines. The droplet internal heat flux is characterized by the temperature distribution across the droplets and must therefore be known. Despite the high relevance of the topic, there has only been little success in measuring the actual temperature distribution inside a micro droplet. Nevertheless, many evaporation models evolved over the years that make certain assumptions about the droplet internal phenomena. Some of the assumptions have been stated as correct, most importantly the presence of the so called Hill-vortex. The friction between gas phase and liquid surface cause a liquid flow inside the droplet. The developed flow field can be described by the Hill-vortex model, introduced by [1]. The vortex inside the droplet leads to an internal liquid circulation and thus to an improved liquid heat transfer [2, 3, 4]. The liquid convection can be globally characterized by the Péclet number (Pe). The dimensionless number describes the ratio of the rate of thermal advection to the rate of thermal diffusion [5]:

$$\mathrm{Pe_l} = \frac{u_\mathrm{s} d}{\alpha_\mathrm{l}} = \underbrace{\frac{\rho_\mathrm{l} u_\mathrm{s} d}{\eta_\mathrm{l}}}_{\mathrm{Re_l}} \cdot \underbrace{\frac{\eta_\mathrm{l}}{\rho_\mathrm{l}\alpha_\mathrm{l}}}_{\mathrm{Pr_l}} = \mathrm{Re_l} \cdot \mathrm{Pr_l}. \tag{1}$$

In this equation [5, 6], d is droplet diameter, α_l is the thermal diffusivity, η_l the dynamic viscosity of the liquid and ρ_l the liquid density. u_s is the surface velocity of the liquid inside the droplet. The droplet surface velocity can be approximated using the droplet friction coefficient c_F for a single spherical droplet, the Reynolds number of the surrounding free-stream gas flow Re_∞ and the dynamic viscosities of the gas phase η_g and B_M is the Spalding mass transfer number, following

$$u_\mathrm{s} = \frac{1}{32} \cdot C_F \cdot \mathrm{Re}_\infty \cdot \frac{\eta_g}{\eta_\mathrm{l}} \qquad \text{with} \qquad C_F = \frac{12.69}{\mathrm{Re}^{2/3} \cdot (1 + B_\mathrm{M})}. \tag{2}$$

The Péclet number may also be expressed by the product of the Reynolds number (Re) and Prandtl number (Pr), where the Reynolds and Prandtl number is calculated by using the physical properties of the liquid of the droplet. However, numerical studies allow an easy assessment of the Péclet number and its influencing parameter. An experimental study of the Hill-vortex on the heat flux and temperature field of smallest micro droplets have by far been limited [4, 7]. Recently, a new Laser-Induced Fluorescence (LIF) method was introduced with the potential to determine droplet internal temperature fast and without much data post processing [8]. The method is called pulsed 2cLIF-EET and has been specifically developed to characterize the temperature field, size and velocity of micro droplet streams by imaging with a negligible effect of motion blur. The basic principle of 2cLIF-EET is similar to conventional 2cLIF thermometry [9], where fluorescence of a temperature sensitive dye is recorded in two color channels after excitation by a laser. The ratio of these two color channels ideally depends on the liquid's temperature

only. The difference to basic 2cLIF is the use of a pulsed laser and a second fluorophore that enables morphology-dependent-resonances (MDRs) enhanced energy transfer (EET) [10]. The pulsed laser is commonly not applied in micro droplet experiments, because of the generation of MDRs and subsequent lasing of the temperature sensitivity fluorophore [11]. The conventional use of a CW laser allows to reduce the effect of MDRs, but also induces a significant effect of motion blur, which makes the use of an imaging setup mostly obsolete. However, MDRs are constructive interference of light that circles around the droplet surface [12]. The consequence is an increased length of stay of the laser light's photons in the droplet and thus a higher photon density [13]. The high photon density favors the probability for stimulated dye emission at the droplet surface. In combination with the spherical droplet cavity, stimulated emission turns into lasing. The droplet virtually becomes a laser with a wavelength that depends on the dye's emission characteristics and the droplet size.[12] Because of the disruptive effect of lasing on 2cLIF thermometry, 2cLIF-EET foresees the use of a second dye [8]. This second dye matches with its absorption spectrum the lasing wavelength of the temperature sensitive dye [14]. Similar to the lasing, radiative energy transfer between the two dyes is enhanced due to the high photon density [15]. The lasing is interrupted by absorption and efficiently transferred via a Stokes-shift by the second dye to much higher wavelengths. As a consequence, capability for 2cLIF thermometry of the first dye is restored [8]. Remaining disruptive effects of spatial variations in the energy transfer rate [16] and self-absorption by the second dye can be corrected by post processing [10, 17].
This work applies the pulsed 2cLIF-EET thermometry method for visualizations of heated n-dodecane droplet streams under different ambient pressures. Goal of this work is to access the two main processes during droplet heating: i) the convective heat transfer from the ambient gas into the droplet and ii) the heat conduction inside the droplet. i) is mainly influenced by the surrounding gas flow. Varying ambient pressures result in an increased gas density and influences the heat exchange with the droplet. ii) is influenced by the heat conduction and a flow inside the droplet imposed by the gas flow. Thus, the advection flow inside the droplet is influenced by the ambient pressure as well. The relation between heat conduction and advection is described by the Péclet number. Both processes are linked at the droplet surface and can't be described completely separate. A comparison with an "effective thermal conductivity (ETC)" model for droplet heating is used to investigate both processes and to disclose imprecisions of the models and the measurement system. n-dodecane is used to minimize liquid evaporation, thus only heat transfer is investigated.

Theory of pulsed 2cLIF-EET thermometry of micro droplets

Pulsed 2cLIF-EET theory is based on conventional 2cLIF theory [18]. The use of a pulsed laser and radiative energy transfer to a second dye is not explicitly modeled. Instead, wavelength dependent (λ) fluorescence intensity I [W] of a small measurement volume with cross-sectional area A and thickness x (laser beam propagation direction) is modeled in accordance with common LIF theory:

$$I(\lambda, x) = K_{\mathrm{opt}}(\lambda) I_0 \phi(\lambda) A \left[1 - \exp\left(-\varepsilon(\lambda) C x\right)\right] \tag{3}$$

In this equation $K_{\mathrm{opt}}(\lambda)$ [-] is an optical constant accounting for the detector's efficiency and the angle of detection, $\varepsilon(\lambda)$ [L/(mol cm)] is the dye's molar attenuation coefficient, C [mol/L] is the combined concentration of both dyes, I_0 [W/m^2] is the dye excitation intensity by the pulsed laser and $\phi(\lambda)$ the quantum yield of the temperature sensitive dye. Similar to basic 2cLIF, equation 3 is linearized, because laser light attenuation is assumed to be negligible [18]. In order to include remaining spatial effects of the radiative energy transfer and self-absorption, a new variable $g(\lambda)$ is introduced:

$$I(\lambda) \approx K_{\mathrm{opt}}(\lambda) I_0 \phi(\lambda) \varepsilon(\lambda) C V g(\lambda) \tag{4}$$

Two parameters, the quantum yield $\phi(\lambda)$ and the molar absorption coefficient $\varepsilon(\lambda)$, are temperature dependent and can be modeled by an Arrhenius approach [18, 17]:

$$I(\lambda) = K_{\mathrm{opt}}(\lambda) K_{\mathrm{spec}}(\lambda) I_0 C V \exp\left(\frac{\beta(\lambda)}{T}\right) g(\lambda) \tag{5}$$

Equation 5 contains $\beta(\lambda)$ [K] as wavelength dependent absolute temperature sensitivity and a new constant $K_{\mathrm{spec}}(\lambda)$ [1/mol] that comprises all spectral properties of the dyes. An integration of equation 5 allows to describe emission in a single color channel (i) from wavelength λ_{i1} to λ_{i2}. Moreover, temperature sensitivity of each color channel can be approximated by a polynomial with coefficients a_{i} and b_{i}.

$$I_i = K_{\mathrm{opt,i}} K_{\mathrm{spec,i}} I_0 C V \exp\left(\frac{a_{\mathrm{i}}}{T^2} + \frac{b_{\mathrm{i}}}{T}\right) g_{\mathrm{i}} \tag{6}$$

According to 2cLIF theory [9], two color channels of spontaneous fluorescence emission are selected. The first channel I_1 is selected in a wavelength region with a low temperature sensitivity, while color channel I_2 is selected with high temperature sensitivity. The ratio R_{12} [$-$] allows to eliminate the direct influences from the measurement volume V, dye excitation intensity I_0 and dye concentration C, but maintains a sufficient dependency on temperature [17]:

$$R_{12} = \frac{I_1}{I_2} = \frac{K_{\mathrm{opt},1} K_{\mathrm{spec},1}}{K_{\mathrm{opt},2} K_{\mathrm{spec},2}} \exp\left(\frac{a_{12}}{T^2} + \frac{b_{12}}{T}\right)\left(\frac{g_1}{g_2}\right) \tag{7}$$

$$= \underbrace{\exp\left(\frac{a_{12}}{T^2} + \frac{b_{12}}{T} + \log(K_{12})\right)}_{f_{12}} \cdot \underbrace{\left(\frac{g_1}{g_2}\right)}_{g_{12}} \tag{8}$$

Summarizing equation 7 allows to describe the intensity ratio in dependency of the two dimensionless functions f_{12} and g_{12}. Function f_{12} requires a temperature calibration under isothermal, non-evaporating conditions to fit temperature dependent polynomial coefficients a_{12} and b_{12} as well as the setup constant K_{12}. During the calibration, images of the droplet ratio-fields R_{12} most like show an inhomogeneous pattern, which should not be present under isothermal conditions. The pattern can be interpreted as the spatial variations of the radiative energy transfer rate and self-absorption across the droplet. The error is independent of temperature and can be isolated by calculating a normalized droplet ratio-field with the average droplet-ratio value $\left(\bar{R}_{12}\right)$. The result corresponds to the function g_{12}=R_{12}/$\bar{R}_{12}$. Function g_{12} is scale-able to other droplet sizes within certain limits [17].
Applying a function g_{12} for corrections of the energy transfer rate and self-absorption is an entirely empirical procedure. This error-mask method is only suitable for droplet stream experiments, where dye concentration and dye excitation intensity undergo only small changes [10].

Experimental setup and data post processing
A vibrating orifice droplet generator (VODG) produces micro droplets. The VODG is equipped with a quartz glass orifice with a cylindrical pinhole with a diameter of 47.1 µm. A piston-pump supplies pressurized liquid for injection through the orifice. The pump is driven by a step-motor, whose rotational speed is regulated to maintain a constant liquid volume flow rate of $\dot{V}_{\mathrm{inj}}$=20 µl/s. The volume flow rate has been cross-checked by additional weighing of collected liquid. A heating cartridge with an integrated thermocouple controls the injection temperature. A surrounding water circuit provides cooling. The liquid breakup is adjusted by a piezo-element that forces a frequency of f=35 kHz onto the liquid jet. The selected frequency stabilizes the breakup wavelength of the injected liquid jet. The consequence is a mono-disperse droplet stream from about 20 to 80 mm downstream the orifice. The injection flow rate and piezo-frequency correspond to an initial droplet diameter of roughly 103.3 µm and an nozzle outlet velocity of approximately 13 m/s.

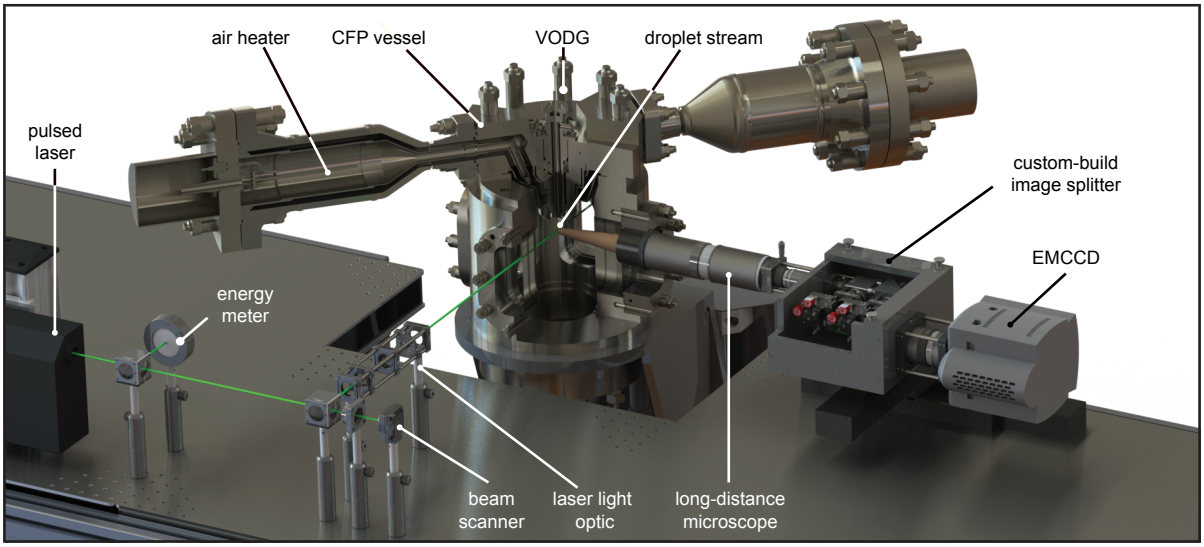

Figure 1. The experimental setup consists of a vibrating orifice droplet generator (VODG) that is positioned in a constant-pressure flow vessel. The dye seeded droplet stream is excited by a pulsed laser and observed tough a long-distance microscope. Received fluorescence emission is separated by wavelength into two color channels. Both color channels are recorded side-by-side with a single EMCCD.

The VODG is positioned centrally in the head of a constant-pressure flow (CPF) vessel with an inner vessel diameter of 120 mm (see Fig. 1). Dry air flows though the vessel from top to bottom with a flow velocity of less than u_{a}=0.014 m/s. Air heaters allow controlling the ambient air temperature. The CPF-vessel is optical accessible by quartz windows with an observable height of the droplet chain of 100 mm. The ambient air temperature reduces about ΔT_{a}=12 K along the observable droplet stream height, due to losses through the chamber walls, windows and cooling circuits inside the window mounts. The temperature distribution in vicinity of the droplet chain is continuously monitored by four thermocouples. Due to the small size of the droplets, imaging of the droplet temperature fields requires a large magnification. As a consequence, the droplet stream connot be investigated entirely in a

single measurement and therefore must be investigated step-wise at discrete positions along its stable propagation length. Single measurement positions are observed by traversing the entire CPF-vessel up or down.
The droplet stream consists of n-dodecane seeded with the fluorophores pyrromethene 597-8C9 (PM597) and Oil Blue N (OBN). n-dodecane is selected due to its particular low volatility. That way, evaporation is expected to be negligible, but heat flux into the droplet is presumably high. PM597 is used as temperature sensitive dye, because it is well dissolved in n-dodecane without a detrimental acid-base reaction and has a low tendency for self-absorption [19]. A dye concentration of C_{PM597}=2 µM is selected to ensure negligible effects of self-absorption, attenuation and most importantly feature a high 2cLIF temperature sensitivity.[1] The dye OBN is spectroscopically well matched to PM597 and enables energy transfer [14]. OBN is almost exclusively excited by energy transfer. Lasing of PM597 due to the pulsed dye excitation is efficiently Stokes-shifted via energy transfer to OBN. OBN-lasing occurs for wavelengths higher than 670 nm, and thereby irrelevant for wavelength regions of 2cLIF thermometry [8]. Unfortunately, OBN has a high tendency for self-absorption and dynamic quenching. Both properties are responsible for the spatially remaining effects of energy transfer that must be corrected using the error-mask method. The dye is dissolved with a concentration of C_{OBN}=0.5 µM to simultaneously ensure a sufficient lasing-shift and maintain a high spontaneous emission intensity of PM597.
An Nd:YAG laser with a pulse duration of 4 ns and a wavelength of 532 nm is used for fluorescence excitation of PM597. The laser beam is reshaped by an array of lenses and apertures to flat-top intensity profile. The laser pulse repetition rate accounts for 2.5 Hz. The specific dye excitation intensity is kept constant throughout the experiments at I_0=2.1 MW/cm^2 (pulse energy 12.75 mJ, beam diameter 14 mm,laser stability deviation $<$3 %).
A custom-build long-distance microscope with a working distance of 125 mm and a numerical aperture of NA=0.37 (corresponding to an optical resolution of about 0.9 µm) collects emission of the droplet stream. After passing the microscope, Mie-scattering light is blocked by a Notch-filter (Thorlabs NF533-17). Remaining emission enters a custom-build image splitter. Fluorescence is separated at a wavelength of 573 nm using a dichroic beam splitter (Chroma ZT561rdc). Each light path is further band-pass filtered: Color channels I_1 has a low central wavelength of 549 nm and is less temperature sensitive than color channel I_2 with a central wavelength of 589 nm. Both color channels feature a full-width half maximum of 15 nm (both Semrock BL). The color channels are selected in accordance with [8, 10]. Fluorescence images of both color channels are recorded side-by-side on a single camera. The camera is an electron-multiplied CCD (EMCCD, Andor iXon3 DU-888) that allows an amplification of the observed fluorescence emission with a gain-factor of 1000 x. The EMCCD sensor is cooled to 178 K for an optimum signal to noise ratio. Recorded fluorescence images of the droplet stream appear on the camera sensor with a magnification of 6.5 x, which corresponds to a scale of 2 µm/px.[2] Thus, images have a height of 2.0 mm, which allows to observe four to five droplets at the same time. The EMCCD is synchronized to the pulsed laser. For each measurement point 500 droplets are recorded and post processed.
Fig. 2 (A) shows two simultaneously recorded images of the two color channels I_1 and I_2 as well as their intensity ratio R_{12}. Droplets are mono-disperse and appear with a Gaussian-like intensity distribution. The inter-droplet distance λ_d is constant of the recorded image and can be utilized to determine the local droplet velocity u, because the breakup frequency f of the injected jet is known: $u = \lambda_d \cdot f$. The ratio-image of the droplet stream shows a low signal to noise ratio, especially at the droplet surface region, where fluorescence intensity is weak and their ratio can produce large measurement errors. Thus, no single droplet temperature measurements can be performed. Instead droplets of many recorded images are extracted and isolated. All isolated droplets are stacked in a matrix and aligned with their centers. Averaging the matrix over its depth leads to an average droplet intensity-ratio image. The ratio-image looks identical to the error-mask image in Fig.2(B).
In order to measure droplet temperature, size and velocity under droplet heating conditions, a previous 2cLIF temperature calibration must be conducted. The calibration foresees a variation of the droplet temperature under isothermal, non-evaporating conditions. Isothermal conditions are provided by keeping the liquid injection and ambient air temperature at the same value. Non-evaporating conditions are difficult to provides, because the constant air flow prohibit saturation of the ambient gas phase. Instead, measurements are simply performed as close as possible to the orifice of the VODG, which lies 30 mm downstream. The calibration has two important results: i) The average error-mask g_{12} (see eq. 8) which is required to correct inhomogeneity of the droplet ratio-field (Fig.2,B) and ii) the average temperature calibration curve (Fig.2,C) that is fitted to the polynomial in the temperature function f_{12} (see eq. 8). The calculated error-mask g_{12} only shows deviations of less than $\pm$3.4 %. This low magnitude is the result of the low dye concentrations (for details see [10]). The slope of the temperature calibration curve allows to quantify the 2cLIF temperature sensitivity with $T_{\mathrm{sens,2cLIF}}$=0.27 %/K. The result matches the expectations, because it exceeds previous experiments with higher dye concentration [10, 17]. The smooth temperature calibration curve and the correction of the error-mask are connected with an average droplet temperature measurement accuracy of 0.5 K. The curves standard deviation correspond to the spatial median absolute deviation accuracy across the droplet, which accounts for approximately 2.5 K.
In this study droplet heating measurements are conducted for n-dodecane with a droplet-starting diameter of around 100 µm, a constant ambient temperature of $T_{\mathrm{a}} = 550$ K and droplets are injected with a starting temperature of $T_{\mathrm{inj}} = 305$ K. The transient behavior of the droplet heating is studied at nine equally spaced axial positions from 30 to 70 mm downstream the VODG's orifice. The droplet flight-time to each position can be calculated under

[1] In general, a lower dye concentration increases the 2cLIF temperature sensitivity of PM597.
[2] The relay-lens system of the image splitter has a magnification of 1 x.

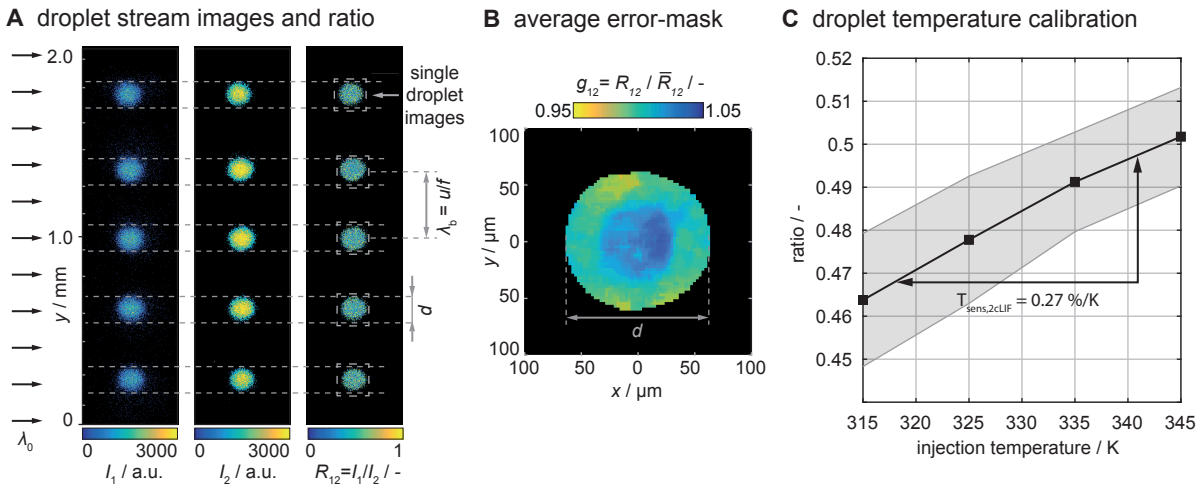

Figure 2. A: images of the intensities of the two color channels I_1 and I_2 (left and middle) and the resulting intensity ratio R_{12} on the right side. The droplets are excited from the left side with laser light. B: shows the independent average error-mask g_{12} to correct spatial deviations in the fluorescence ratio due to self-absorption and energy transfer. C: shows the dependency between intensity ratio and temperature. The measurements are done under isothermal conditions and the curve is used for temperature calibration of the system. The slope of the graph is indicating the temperature sensitivity.

consideration of the local droplet velocity, following

$$t = \int_{h_0}^{h} \frac{1}{u(y)} \, \mathrm{d}y \tag{9}$$

where h is the distance to the outlet and $u(y)$ the determined velocity at the axial position y. The droplet heating experiments comprise two different ambient pressures of $p_{\mathrm{a},1}$=1.39 bar and $p_{\mathrm{a},2}$=2.11 bar. The different ambient pressures allow a variation of the Péclet-number, without much influence on the droplet conditions itself. Only the droplet velocity is changing due to the elevated ambient density, which in turn affects the heat transfer from gas to droplet. However, droplet size and heating potential (constant ambient temperature) remain constant.

Results

Besides droplet temperature distribution, the system determines the droplet diameter and droplet velocities at the measuring position. A trend with respect to evaporation time can be derived. Figure 3A shows the droplet diameter versus the evaporation time. The diameter is increasing at the beginning due to a decreasing fluid density and negligible evaporation. At later times the diameter is declining because of starting evaporation, but overall the evaporation is with 0.02 % still negligible. The increased pressure leads to an earlier swelling of the droplet, but an enhanced evaporation cannot be observed. The droplet velocities for both ambient pressures are shown in figure 3B. The droplet velocity is approximately linear decreasing in both cases. A higher pressure leads to a higher deceleration due to increased ambient density and higher friction. Figure 3C shows the mean droplet temperatures

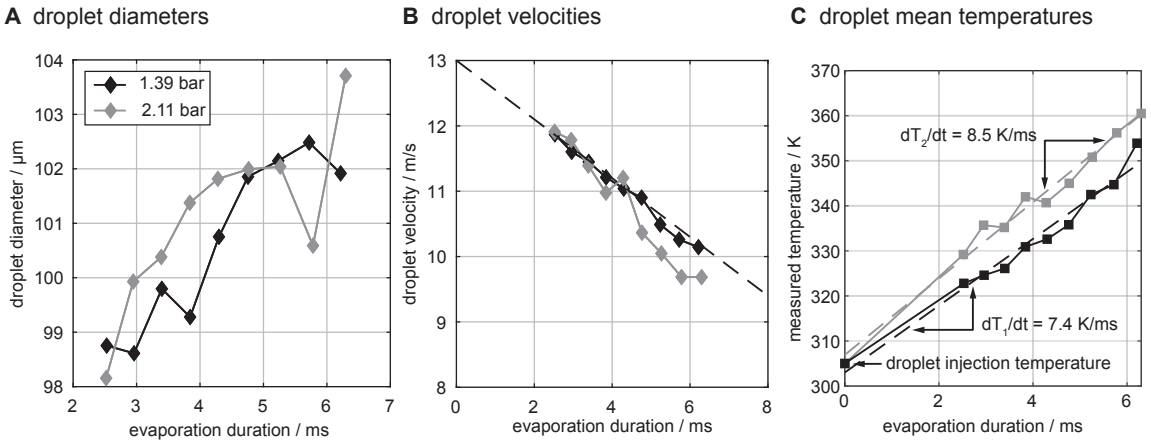

Figure 3. A: measured droplet velocities for ambient pressure of $p_{\mathrm{a},1} = 1.39\,\mathrm{bar}$ (1.) and $p_{\mathrm{a},2} = 2.11\,\mathrm{bar}$ (2.). B: Temporal evolution of mean droplet temperature for both ambient pressures.

with respect to the evaporation duration. The droplet temperature is increasing with a constant gradient (linear) due to the negligible amount of evaporation. In the following the gradient will be denote as heating rate. For an ambient

pressure of $p_{\mathrm{a},1} = 1.39\,\mathrm{bar}$ the heating rate is 7.4 K/ms and for $p_{\mathrm{a},2} = 2.11\,\mathrm{bar}$ 8.5 K/ms. The heating rate can be seen as a measure of the heat flux into the droplet. The ratio of both heating rates is 1.149 and thus the heat transfer is increased by around 15 % with an increase of ambient pressure of 52 %. The convective heat transfer for a spherical droplet can be described by a function of Reynolds and Prandtl number. The ratio of the Nusselt number for both ambient pressure [5, 20] can be be estimated with the well-established Ranz-Marshall equation for non-evaporating conditions ($B_M = 0$):

$$\frac{\overline{\mathrm{Nu}_2}}{\overline{\mathrm{Nu}_1}} = \frac{2 + 0.6\overline{\mathrm{Re}}_{\mathrm{g},2}{}^{\frac{1}{2}}\overline{\mathrm{Pr}}_{\mathrm{g},1}{}^{\frac{1}{3}}}{2 + 0.6\overline{\mathrm{Re}}_{\mathrm{g},1}{}^{\frac{1}{2}}\overline{\mathrm{Pr}}_{\mathrm{g},1}{}^{\frac{1}{3}}} = 1.136 \tag{10}$$

and predicts an around 14 % higher convective heat transfer for $p_{\mathrm{a},2} = 2.11\,\mathrm{bar}$, what is in good agreement with the measurements.

Additional to the droplet mean temperature the system enables the measuring of temperature fields inside the droplet. Especially for planar temperature measurements a few characteristics of the measurement system has to be mentioned. The temperature images are a two dimensional projection of a three dimensional body and cannot be interpreted as a cross section of the temperature field. Each pixel of the temperature image is based on integral measurements of the fluorescence intensities on both wavelength bands and thus the image can be interpreted as an average temperature along the droplet depth. Hence, the center of the image does not describe the core temperature of the droplet. It comprise the whole signal along the droplet depths. Because of the influence of the warmer droplet surface temperature, the system is overestimating the temperature of the droplet core. With increasing distance from the droplet center the integral length (droplet depth) is decreasing and the averaging effect becomes weaker. Theoretically, at the border of the droplet the measurements should only describe the surface temperature. Unfortunately, due to the small droplet depth at the droplet border the fluorescence signal is weak. Hence, the signal-to-noise ratio becomes worse. Furthermore, due to the magnification of the microscope lens the depth of field is smaller than the droplet diameter. The position of the object plane inside the droplet is influencing the integral temperature measuring. Because of that, movements of the droplet stream in direction of the optical axis can have a significant effect on the temperature measurement. Conclusively, the averaging effect is leading to an overestimation of the temperature (especially at the droplet core) and deviations of the object plane inside the droplet can introduce further errors in the temperature measurements and droplet size determination. Because of the averaging along all three spatial directions the mean droplet temperature is more reliable.

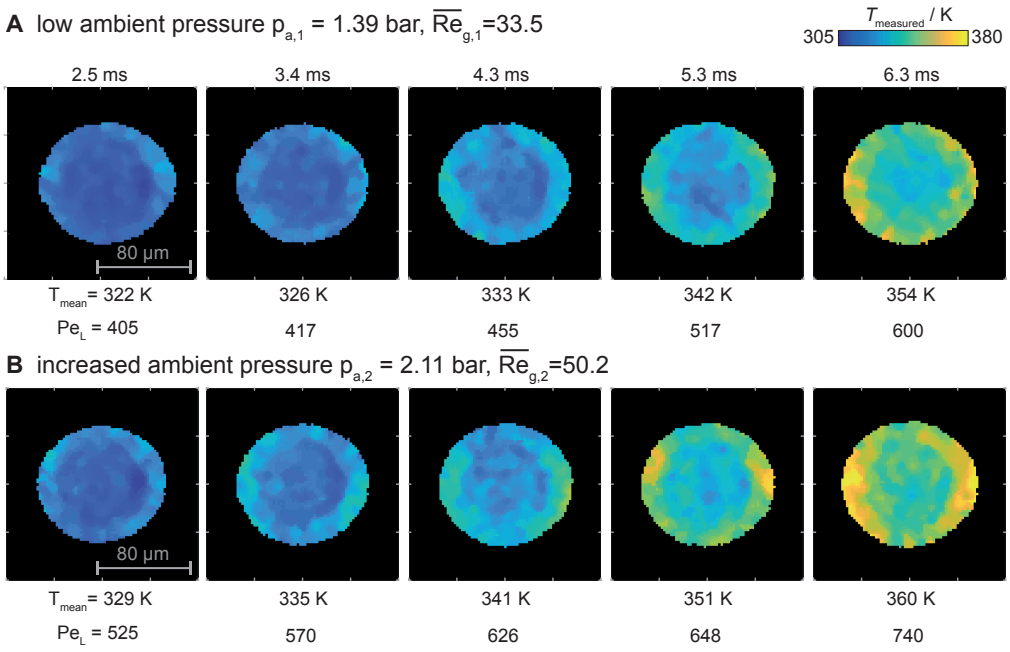

Figure 4. Temporal and spatial evolution of the droplet temperature fields inside the droplets. A: temperature images for an ambient pressure of $p_{a,1}$ =1.39 bar. B: temperature images for $p_{a,2}$ =2.11 bar.

Figure 4 shows the temporal and spatial evolution of the temperature fields. As expected, after short heating time the temperature distribution is still homogeneous but at later times the surface temperatures are increasing stronger than the droplet center. The temperature distribution along the droplet surface shows an increased temperature at the right and left side of the droplet at later times. This is contrarily to the theory of convective heat transfer around a spherical droplet, which predicts the highest local transfer coefficient around the stagnation point of the flow and in the wake region downstream. This deviation may be induced by the disturbances of the flow by previous droplets, which are leading to higher gas velocities at both sides of the droplet. For high droplet Péclet numbers ($\mathrm{Pe_l} > 200$) the fluid circulation inside the droplet should be fully developed and the isothermals and streamlines should be the same [5]. The instantaneous Péclet numbers are indicated below the temperature images. The shown Péclet

numbers are valid for a single moving droplet and they do not take the influence of previous droplets into account. The typical structure of a Hill-vortex inside the droplet cannot be seen in the images. As shown by [21], the Péclet number for the droplet stream is much lower (magnitude around 50) compared to a single droplet (magnitude around 500). Due to the low Péclet number the Hill-vortex is not developed in the conducted experiments. Furthermore, [22] showed for a $\mathrm{Pe} = 200$ that the Hill-vortex only starts to develop after 0.1 s.
For a comparison with the measurements, the "effective thermal conductivity" (ETC) model is used, described in detail in [5, 20, 23]. It is a simplified vortex model, where disruptive surface tension effects, i.e. the Marangoni effect and the deformation of the droplet, are neglected. The improved liquid heat transfer by the Hill-vortex is included by a Péclet number dependent adhoc factor. This simplification allows to assume radial symmetry of the droplet and the droplet temperature field, which leads consequently to an uniform surface temperature. The extended film model, suggested by [5], is used to describe the convective transport processes. The ETC-model is only designed for a single droplet and not for droplet streams, where flow and vapor fields are disturbed by previous droplets. Therefore, the Nusselt number is corrected with the factor $\eta(C)$ based on the dimensionless droplet distance $C = {}^{\lambda_b}/_{d}$ for $C > 3$, as described by [24]. It is defined as,

$$\eta(C) = \tanh\left(0.36 \cdot C - 0.82\right). \tag{11}$$

Additionally to the mean droplet temperature, the droplet surface temperature and the droplet core temperature are extracted from the temperature images. The surface temperature is averaged for droplet pixels with radial positions $> 0.85d$ and the core temperature is averaged for pixels $< 0.15d$. The radial averaging thicknesses are in agreement with the radial resolution of the model. Figure 5 shows the measurement results for both ambient

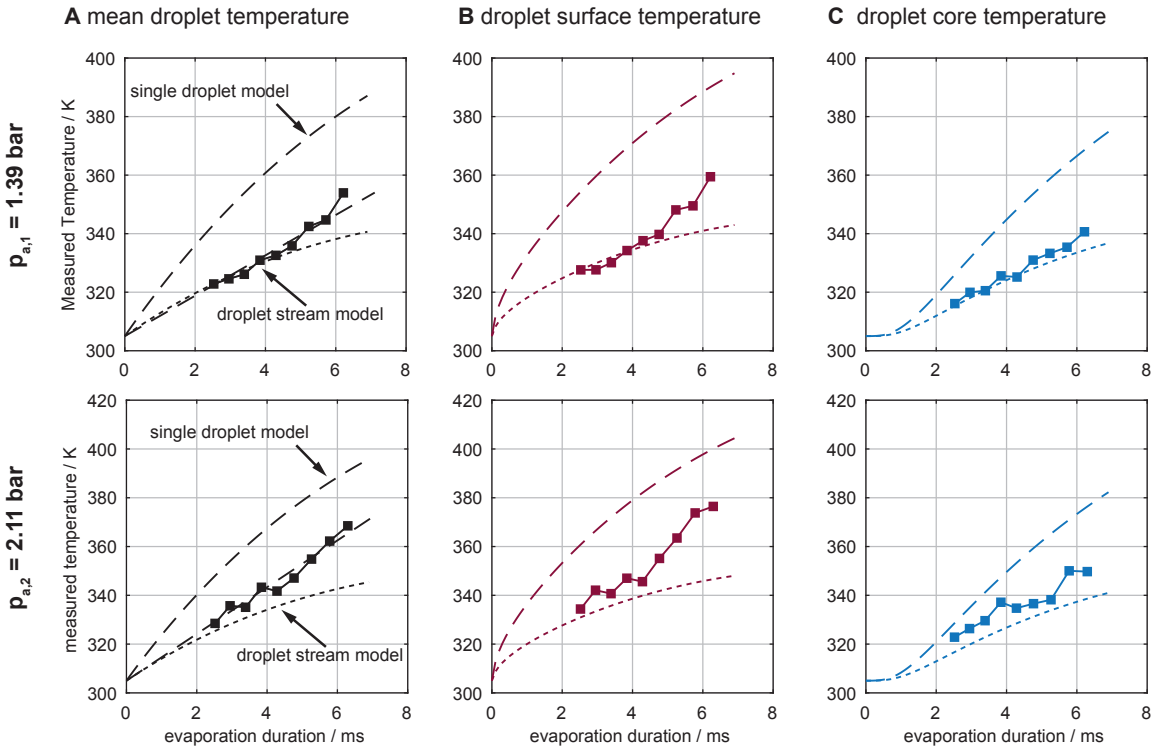

Figure 5. Temporal evolution of the droplet temperature and comparison with simulation models for heated single droplets and monodisperse droplet streams. Mean droplet (A), droplet surface (B) and the droplet core temperature (C) for an ambient pressure of $p_{\mathrm{a},1} = 1.39\,\mathrm{bar}$ (top row) and $p_{\mathrm{a},2} = 2.11\,\mathrm{bar}$ (bottom row). The droplet surface temperature is averaged for radial positions between $0.85 \cdot d$ and d (d is the droplet diameter). The core temperature is averaged for radii smaller than $0.15 \cdot d$

pressures in comparison to the ETC-models for a single droplet and a droplet stream. The mean droplet temperature is averaged over the droplet volume. The measurements for an ambient pressure of $p_{\mathrm{a},1} = 1.39\,\mathrm{bar}$ are in good agreement with the droplet stream model until an evaporation duration of 5 ms (max. $\Delta T = 3\,\mathrm{K}$). After this time the droplet stream model underestimates the droplet temperature. Basically, this could be explained with the integral characteristics of the temperature measurement along the droplet depth, but this would lead to a deviation for all data points. Contrarily to the linear trend of the measurements, the model is predicting at later timings a declining temperature gradient. The correction factor for the Nusselt number (equation 11) in the droplet stream model is only valid for a dimensionless droplet distance greater than three. After five milliseconds the droplets distance is falling bellow this threshold and may causes the deviations of up to 19.5 K.
For the increased ambient pressure, the droplet stream model prediction are becoming worse and is increasing from 3 K (2.5 ms) to 17 K (6.3 ms) for the mean droplet temperature. The measured temperatures are lower than the predicted single droplet and above the droplet stream predictions but still in a reasonable range. Conclusively the deviation between ETC-model and measurements could be based on inaccuracies of measurement system or an imprecisely description of the pressure dependency of the heat transfer in the ETC-model.

Conclusions

The presented improved 2cLIF system with application of a pulsed laser allows for the first time resolved temperature field measurements across entire micro droplets with diameters of 100 μm and below. In the past this was prevented by the occurrence of MDRs and subsequent lasing of the temperature sensitive fluorophore. Enhanced energy transfer shifts the lasing to higher wavelength and restore the temperature sensitivity of the fluorophore. The achieved average droplet temperature accuracy is 0.5 K and a spatial median absolute deviation of 2.5 K.

The new system is used to investigate heating of a n-dodecane droplet stream moving in an isothermal atmosphere under two different ambient pressures. Due to the low vapor pressure of n-dodecane evaporation of the droplets is negligible. Thus the study is focused on heat transfer. The mean droplet temperature measured with the system is used to describe the convective heat transfer. The heating rates are increasing from 7.4 $^{K}/_{ms}$ to 8.5 $^{K}/_{ms}$ by an increase of 52 % in ambient pressure. This ratio scales with the ratio of the Nusselt number of a spherical droplet.

Furthermore, the temperature measurements are compared with heating models for single droplets and droplet streams. The temperatures are overestimated by the single droplet model, what is reasonable due to the influence of previous droplets. The droplet stream model considers these effects and offers a good prediction for low ambient pressures but underestimates the temperature of the droplets for an elevated ambient pressure. Besides the mean droplet temperature, the system is used to visualize the temperature distribution inside the droplet. It is shown that an elevated density increase the convective heat transferred from the ambient gas to the droplet and the internal heat conduction. The results in comparison to the models reveal the plausibility of the introduction of the "effective thermal conductivity model", which takes the flow inside the droplet into account. The temperature distributions do not show the Hill-vortex structure.

The final objective, to measure planar temperature fields in cross sections of micro droplets, is not reached yet. Due to the integral measuring effect along the droplet depth, the results are still not resolved in all three spatial dimensions. Furthermore, a moving droplet stream can lead to further errors in temperature and droplet diameter determination, which are hardly to predict and to correct. Against the background it is possible that the three dimensional structure of the Hill-vortex cannot be resolved by the actual measurement system.

Acknowledgement

This work was funded by the Deutsche Forschungsgemeinschaft (DFG, German Research Foundation) under Germany's Excellence Strategy - Cluster of Excellence 2186 "The Fuel Science Center" - ID: 390919832.

References

[1] R. Kronig and J. C. Brink. *Applied Scientific Research*, 2(1):142, Jan 1951.
[2] S. Prakash and W.A. Sirignano. *International Journal of Heat and Mass Transfer*, 21(7):885 – 895, 1978.
[3] W. A. Sirignano. Cambridge University Press, Cambridge, 1999.
[4] G. Castanet, A. Labergue, and F. Lemoine. *International Journal of Thermal Sciences*, 50(7):1181–1190, 2011.
[5] B. Abramzon and W. A. Sirignano. *International Journal of Heat and Mass Transfer*, 32(9):1605–1618, 1989.
[6] B. Abramzon and S. Sazhin. *Fuel*, 85(1):32–46, 2006.
[7] Guillaume Castanet, Alain Delconte, Fabrice Lemoine, Loïc Mees, and Gèrard Gréhan. *Experiments in Fluids*, 39(2):431–440, 2005.
[8] Johannes Palmer, Manuel A. Reddemann, Valeri Kirsch, and Reinhold Kneer. *Experiments in Fluids*, 57(12), 2016.
[9] P. Lavieille, F. Lemoine, G. Lavergne, J. F. Virepinte, and M. Lebouché. *Experiments in Fluids*, 29(5):429–437, 2000.
[10] Johannes Palmer, Manuel A. Reddemann, Valeri Kirsch, and Reinhold Kneer. *Experiments in Fluids*, 59(6):943, 2018.
[11] Fabrice Lemoine and Guillaume Castanet. *Experiments in Fluids*, 54(7):1–34, 2013.
[12] Gang Chen, Md. Mohiuddin Mazumder, Richard K. Chang, J. Christian Swindal, and William P. Acker. *Progress in Energy and Combustion Science*, 22(2):163–188, 1996.
[13] R. K. Chang and P. W. Barber, editors. Advanced Series in Applied Physics. WORLD SCIENTIFIC, 1988.
[14] Lionel Perrin, Guillaume Castanet, and Fabrice Lemoine. *Experiments in Fluids*, 56(2), 2015.
[15] L. M. Folan, S. Arnold, and S. D. Druger. *Chemical Physics Letters*, 118(3):322–327, 1985.
[16] S. Arnold. *The Journal of Chemical Physics*, 104(19):7741, 1996.
[17] Johannes Palmer, Manuel A. Reddemann, Valeri Kirsch, and Reinhold Kneer. *Experiments in Fluids*, 59(3):263, 2018.
[18] F. Lemoine, Y. Antoine, M. Wolff, and M. Lebouche. *Experiments in Fluids*, 26(4):315–323, 1999.
[19] V. Deprédurand, P. Miron, A. Labergue, M. Wolff, G. Castanet, and F. Lemoine. *Measurement Science and Technology*, 19(10):105403, 2008.
[20] Sergei S. Sazhin. *Progress in Energy and Combustion Science*, 32(2):162–214, 2006.
[21] G. Castanet, L. Perrin, O. Caballina, and F. Lemoine. *International Journal of Heat and Mass Transfer*, 93:788 – 802, 2016.
[22] T. V. Binu and S. Jayanti. *Thermal Science and Engineering Progress*, 8:385–396, 2018.
[23] S. S. Sazhin, A. Elwardany, P. A. Krutitskii, G. Castanet, F. Lemoine, E. M. Sazhina, and M. R. Heikal. *International Journal of Heat and Mass Transfer*, 53(21-22):4495–4505, 2010.
[24] C. Maqua, G. Castanet, F. Grisch, F. Lemoine, T. Kristyadi, and S. S. Sazhin. *International Journal of Heat and Mass Transfer*, 51(15-16):3932–3945, 2008.